JM PAPERS

Off-centre gravity induces large-scale flow patterns in spherical Rayleigh–Bénard convection

Guiquan Wang[1,†], Luca Santelli[2], Roberto Verzicco[1,2,3], Detlef Lohse[1,4] and Richard J.A.M. Stevens[1,†]

[1]Physics of Fluids Group and Twente Max Planck Center, Department of Science and Technology, Mesa+ Institute, and J. M. Burgers Center for Fluid Dynamics, University of Twente, P.O. Box 217, 7500 AE Enschede, The Netherlands

[2]Gran Sasso Science Institute, Viale F. Crispi 7, 67100 L'Aquila, Italy

[3]Dipartimento di Ingegneria Industriale, University of Rome' Tor Vergata', Via del Politecnico 1, 00133 Rome, Italy

[4]Max Planck Institute for Dynamics and Self-Organization, Am Fassberg 17, 37077 Göttingen, Germany

We perform direct numerical simulations to study the effect of the gravity centre offset in spherical Rayleigh–Bénard convection. When the gravity centre is shifted towards the south, we find that the shift of the gravity centre has a pronounced influence on the flow structures. At low Rayleigh number Ra, a steady-state large-scale meridional circulation induced by the baroclinic imbalance, created by the misalignment of the gravity potentials and isotherms, is formed. At high Ra, an energetic jet is created on the northern side of the inner sphere that is directed towards the outer sphere. The large-scale circulation induces a strong co-latitudinal dependence in the local heat flux. Nevertheless, the global heat flux is not affected by the changes in the large-scale flow organization induced by the gravity centre offset.

Key words: Bénard convection, turbulent convection, plumes/thermals

† Email addresses for correspondence: gwang4academy@gmail.com, r.j.a.m.stevens@utwente.nl

G. Wang, L. Santelli, R. Verzicco, D. Lohse and R.J.A.M. Stevens

1. Introduction

The effect of an off-centre gravity location on the flow structures in turbulent thermal convection has not been studied previously. Here, we use spherical Rayleigh–Bénard (RB) convection as an idealized model system to study the effect of an off-centre gravity location on thermal convection in a spherical system. The system consists of a fluid layer enclosed between two spherical shells, heated from the inner sphere and cooled from the outer one. Convection in spherical shells differs from the classical RB convection (Ahlers, Grossmann & Lohse 2009; Lohse & Xia 2010; Chillà & Schumacher 2012) owing to the curvature of the boundaries, non-uniform gravity, and the geometrical asymmetry between the boundary layer at the inner and outer spheres (Busse 1970; Spiegel 1971; Jarvis, Glatzmaierand & Vangelov 1995; Tilgner 1996; Shahnas *et al.* 2008; Deschamps, Tackley & Nakagawa 2010; O'Farrell, Lowman & Bunge 2013; Gastine, Wicht & Aurnou 2015).

Most studies on spherical RB convection focus on the case in which the gravity centre coincides with the geometric one. Busse (1975) used perturbation analysis to show the qualitative difference between convective flow patterns of odd and even spherical harmonic order just above the onset of convection. Subsequently, in an infinite Prandtl number (*Pr*) fluid with application to mantle convection, Bercovici, Schubert & Glatzmaier (1989) showed that these convective patterns persist for Rayleigh numbers (*Ra*) up to 100 times larger than the critical value. For $Ra > 10^5$, the axisymmetric convective patterns break down when the flow starts to show time-dependent behaviour (Iwase & Honda 1997; Deschamps *et al.* 2010; Futterer *et al.* 2013; Yanagisawa, Kameyama & Ogawa 2016). In spherical RB convection, the influence of curvature is important. For constant *Ra*, the length scale of the preferentially convective patterns decreases with increasing radius ratio (Deschamps *et al.* 2010). Yanagisawa & Yamagishi (2005) find that the convective rolls become smaller with increasing *Ra* when the radius ratio is kept constant. Gastine *et al.* (2015) show that for $Pr = 1$, sheet-like thermal plumes are formed near the inner and outer spheres, and these plumes undergo morphological changes into mushroom-like plumes when they eject from the boundary layers to the bulk. These plume dynamics are similar to the situation for classic RB convection (Puthenveettil & Arakeri 2005; Shishkina & Wagner 2008; Zhou & Xia 2010; Chillà & Schumacher 2012). However, due to the asymmetries between the hot and cold surfaces in spherical shells, the mushroom-like plumes emitted from the outer sphere are thicker than those emitted from the inner sphere (Gastine *et al.* 2015). Nevertheless, studies have shown that there are similarities between spherical and classical planar RB convection. For example, Gastine *et al.* (2015) showed that the effective heat transport (characterized by the Nusselt number *Nu*) scaling exponent α in $Nu \sim Ra^\alpha$ in spherical RB convection has a similar *Ra* number dependence as in planar RB convection, where for $Ra \lesssim 10^{11}$, typically $0.28 \lesssim \alpha \lesssim 0.31$ (Ahlers *et al.* 2009).

However, the misalignment between the gravity centre and the geometric one in the spherical RB convection set-up has been overlooked to date. In this study, we use three-dimensional direct numerical simulations to investigate the effect of the gravity centre offset on the flow structures and heat transfer in spherical RB convection. The paper is organized as follows. In § 2, we explain the numerical method and discuss the considered parameter regime. In §§ 3.1–3.3, we discuss the large-scale flow pattern induced by the off-centre gravity. The effect of the large-scale structure on heat transfer is shown in § 3.4. In § 3.5, we study the effect of the gravity profile and *Ra* on flow structures and heat transfer. The paper ends with a summary of our findings and conclusions in § 4.
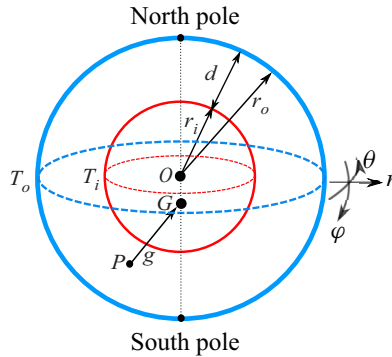
Figure 1. Schematic of spherical RB convection in between two concentric spheres with radius ratio $\eta = r_i/r_o$ between the inner and outer sphere, and gap size $d = r_o - r_i$. A no-slip boundary condition with constant temperature is used on the inner (hot) and outer (cold) sphere. In spherical coordinates the longitudinal, co-latitudinal and radial directions are represented by $\hat{\theta}$, $\hat{\varphi}$ and $\hat{r}$, respectively. The gravity centre G is offset from the geometric centre O, and P is an arbitrary fluid point in the spherical shell.

2. Numerical method and parameters

2.1. *Set-up of convection in spherical shells*

The spherical RB geometry is illustrated schematically in figure 1. Fluid fills a spherical shell between the inner sphere of radius r_i and the outer sphere of radius r_o. The radius ratio between the inner and outer spheres is given by

$$\eta = r_i/r_o. \tag{2.1}$$

In this study, we consider a fixed aspect ratio $\eta = 0.3$. The surface temperatures of the inner and outer spheres are kept constant at T_i and T_o, respectively, with $T_i > T_o$. No-slip boundary conditions are imposed on both boundaries. Point G indicates the gravity centre, which is offset from the geometric centre O. The gravity shift is defined as

$$\varepsilon = |OG|/r_i, \tag{2.2}$$

where $|OG|$ indicates the displacement of the gravity compared to the geometrical centre; see figure 1. In the absence of rotation (and magnetic field), for a sphere, there are no north and south directions, therefore any diametrically opposite symmetry is equivalent to another. Nevertheless, since the spherical coordinates are naturally clustered around the polar axis, it is beneficial to consider the jet aligned along this axis, referred to as north–south, from a computation point of view. For convenience, we always shift the gravity centre G to the south.

The dynamics of spherical RB convection is controlled by the Rayleigh and Prandtl numbers

$$Ra = \frac{\beta g_o \,\Delta T \, d^3}{\kappa \nu}, \quad Pr = \frac{\nu}{\kappa}, \tag{2.3a,b}$$

where β is the thermal expansion coefficient, g_o is the surface-averaged gravity at the outer sphere, ν is the kinematic viscosity, and κ is the thermal diffusivity. We normalize the fields and distances by the length scale $d = r_o - r_i$, the temperature difference ΔT between the inner and outer spheres, and the free-fall velocity $U = \sqrt{\beta g_o \,\Delta T \, d}$.

2.2. *Underlying dynamical equation and numerical method*

We solve the Navier–Stokes equations under the Boussinesq approximation in spherical coordinates, which in dimensionless form read

$$\frac{\partial \boldsymbol{u}}{\partial t} + \boldsymbol{u} \cdot \boldsymbol{\nabla} \boldsymbol{u} = -\boldsymbol{\nabla} p + \sqrt{\frac{Pr}{Ra}} \, \nabla^2 \boldsymbol{u} + C_g g T, \quad \boldsymbol{\nabla} \cdot \boldsymbol{u} = 0, \qquad (2.4)$$

$$\frac{\partial T}{\partial t} + \boldsymbol{u} \cdot \boldsymbol{\nabla} T = \frac{1}{\sqrt{Ra\,Pr}} \, \nabla^2 T, \qquad (2.5)$$

where $\boldsymbol{u}$, p, T and $C_g g$ denote the fluid velocity, pressure, temperature and gravitational acceleration acting in the three directions. The coefficients $C_{g,i}$ (where $i = 1, 2, 3$ correspond to the $\hat{\theta}$, $\hat{r}$ and $\hat{\varphi}$ directions, respectively) denote the decomposition of g, which is detailed in Appendix A. Since we always shift the gravity centre G to the south, the three components of the buoyancy coefficient can be written as

$$C_g g = (0, r + r_i \varepsilon \cos \varphi, -\varepsilon r_i \sin \varphi) \, r_o^{-n_g} L_{GP}^{n_g - 1}, \qquad (2.6)$$

in which $L_{GP} = |\boldsymbol{GP}|$ indicates the distance between a fluid point and the gravity centre; see figure 1. We consider the gravity profile

$$g = (L_{GP}/r_o)^{n_g}, \qquad (2.7)$$

and we use $n_g = -2, -1, 0$ and 1. The value of n_g can be inferred by physical considerations on the mass ratio between the nucleus ($r < r_i$) and the spherical shell ($r_i < r < r_o$). The gravity is constant ($n_g = 0$) when the mass of the spherical shell is negligible. This assumption is typically used to model the Earth's mantle (Bercovici *et al.* 1989). If the mass is condensed centrally, then one obtains $n_g = -2$. Gastine *et al.* (2015) showed that only for this gravity distribution function is there an analytical relation between the viscous dissipation rate (ϵ_U) and Nu, i.e. $\epsilon_U = (3/(1 + \eta + \eta^2))(1/Pr)(Nu - 1)$. When the density is constant within the fluid layer, and no mass is contained in the inner sphere, gravity is directly proportional to the radial coordinate r ($n_g = 1$) (Tilgner 1996).

The governing equations (2.4) and (2.5) are discretized by a staggered central second-order finite-difference scheme in spherical coordinates. The numerical scheme is based on the method by Verzicco & Orlandi (1996), which has been extended recently to spherical coordinates by Santelli, Orlandi & Verzicco (2021). The advantage of this scheme is that it allows arbitrary non-uniform grids in the radial and co-latitudinal directions. Here, it is worthwhile to mention that singularities at the poles are prevented by introducing a new set of quantities $(u_\theta, u_r r^2, u_\varphi \sin \varphi)$, which results in trivial boundary conditions $u_\varphi \sin \varphi = 0$ at the north pole ($\varphi = 0$) and south pole ($\varphi = \pi$) in the co-latitudinal direction. The code has been validated carefully by Santelli *et al.* (2021), and we refer to that work for details on the method. For additional validation results relevant to the flows considered here, we refer the reader to Appendix B.

2.3. *Choice of parameters*

To study the effect of the gravity centre location on the flow dynamics in spherical RB convection, we considered different gravity distributions ($n_g \in \{-2, -1, 0, 1\}$, see (2.7)) and gravity centre offset (ε from 0 to 0.8, see (2.2)) for $Ra = 10^7$ and 10^8. All simulations in this study are for $Pr = 1$. To ensure that the flow is resolved fully, we place a sufficient number of computational grid points in the bulk and the boundary

layers (Stevens, Verzicco & Lohse 2010). As we will use spectral analysis to study the flow structures, we use a uniform grid in the longitudinal and co-latitudinal directions. In the radial direction, the grid cells are clustered towards the inner and outer spheres to ensure that the boundary layers are resolved adequately (Shishkina *et al.* 2010).

We calculate the Nusselt number Nu from the normalized averaged temperature gradients at the inner and outer spheres as follows:

$$Nu_i = -\eta \left.\frac{d\overline{\langle T \rangle_{\theta,\varphi}}}{dr}\right|_{r_i}, \quad Nu_o = -\frac{1}{\eta}\left.\frac{d\overline{\langle T \rangle_{\theta,\varphi}}}{dr}\right|_{r_o}. \tag{2.8a,b}$$

Here, $\langle \cdots \rangle_{\theta,\varphi}$ represents the average over a spherical surface with fixed r, and $\overline{\cdots}$ indicates a time average. Also, Nu_i and Nu_o as functions of the co-latitudinal direction are defined as

$$Nu_i(\varphi) = -\eta \left.\frac{d\overline{\langle T \rangle_\theta}}{dr}\right|_{r_i}, \quad Nu_o(\varphi) = -\frac{1}{\eta}\left.\frac{d\overline{\langle T \rangle_\theta}}{dr}\right|_{r_o}, \tag{2.9a,b}$$

where $\langle \cdots \rangle_\theta$ represents the average over the azimuthal direction. The difference in Nu values obtained at the inner and outer spheres is always less than 0.2 %. Also, we verify that Nu calculated at the spheres is the same as the value obtained from the volume-averaged Nusselt number Nu_v, which is calculated from the surface-averaged Nusselt number Nu_h averaged over concentric spherical surfaces with fixed r, with

$$Nu_h(r) = \frac{\sqrt{Ra\,Pr}\,\langle u_r T \rangle_{\theta,\varphi} - \partial_r \langle T \rangle_{\theta,\varphi}}{-\partial_r T_c}, \tag{2.10}$$

where $T_c(r) = \eta/[(1-\eta)^2 r] - \eta/(1-\eta)$ is the purely conductive temperature profile for constant temperature boundary conditions. Subsequently, we perform radial integration and time averaging to obtain Nu_v as

$$Nu_v = \overline{\frac{1}{d}\int_{r_i}^{r_o} Nu_h(r)\,dr}. \tag{2.11}$$

The volume-averaged root-mean-square (r.m.s.) Reynolds number is given by

$$Re_{rms} = \sqrt{Ra/Pr}\,\overline{\sqrt{\langle u_i u_i \rangle}}, \quad i = 1, 2, 3. \tag{2.12}$$

Here, $\langle \cdots \rangle$ denotes the average over the whole volume of the spherical shell. The details of the simulations considered in this study are summarized in table 1.

3. Results

Before we discuss the turbulent flows in §§ 3.2–3.5, we first focus on the large-scale circulation formation induced by off-centre gravity in a steady axisymmetric flow obtained at $Ra = 10^3$. As indicated in (2.6), the radial and co-latitudinal buoyancy coefficients depend on the gravity centre offset ε and the gravity distribution n_g. To disentangle these effects, for turbulent flows we first examine the effect of the gravity centre offset for constant gravity ($n_g = 0$) at $Ra = 10^8$ in §§ 3.2–3.4. The effect of n_g and Ra is studied in § 3.5.

Ra	n_g	$N_\theta \times N_r \times N_\varphi$	ε	Nu	Nu_v	Re_{rms}
10^6	0	$241 \times 71 \times 121$	0.01	4.89	4.88	151.4
			0.05	4.86	4.86	152.6
10^7	-2	$501 \times 101 \times 251$	0	16.09	16.05	919.5
			0.2	16.18	16.17	965.7
			0.4	16.23	16.22	976.9
			0.8	16.20	16.08	936.8
10^7	-1	$401 \times 91 \times 201$	0	11.89	11.90	657.5
			0.2	11.91	11.89	692.5
			0.4	11.96	11.95	702.6
			0.8	11.41	11.14	526.6
10^7	0	$301 \times 81 \times 151$	0	8.73	8.77	485.6
			0.01	8.92	8.91	486.1
			0.05	8.94	8.93	493.6
			0.2	8.91	8.91	497.6
			0.4	8.97	8.96	494.4
			0.8	8.81	8.74	409.3
10^7	1	$321 \times 85 \times 161$	0	7.04	7.05	358.4
			0.2	6.93	6.89	356.3
			0.4	7.06	7.03	359.5
			0.8	7.10	7.06	319.4
10^8	0	$501 \times 101 \times 251$	0	17.36	17.38	1487.3
			0.01	17.36	17.35	1487.9
			0.05	17.37	17.42	1501.1
			0.1	17.30	17.29	1505.2
			0.2	17.15	17.15	1529.0
			0.4	17.31	17.24	1513.7
			0.8	16.62	16.53	1302.8

Table 1. Details of the simulations. The columns from left to right indicate: *Ra*, the gravity profile exponent n_g (see (2.7)); the number of grid points in the longitudinal, radial and co-latitudinal directions, $N_\theta \times N_r \times N_\phi$; the shift of the gravity centre with respect to the geometrical centre ε (see (2.1)); the average heat transfer *Nu* across the inner Nu_i and outer Nu_o spheres (see (2.8*a,b*)); Nu_v (see (2.11)); and Re_{rms} (see (2.12)).

3.1. *Dynamics of steady flow*

When the gravity centre offsets with the geometric one in spherical RB convection, the crossing between temperature gradient (∇T) and gravitational acceleration ($\boldsymbol{g}$) results in the baroclinic torque, which plays an important role in the generation of vorticity by density variations. Figure 2(*a*) shows gravitational potential isolines to intersect the isotherms in an axisymmetric flow. The curl of the buoyancy term ($\nabla \times \boldsymbol{g}T$) denotes the Boussinesq baroclinic torque under the Boussinesq approximation (Schladow, Patterson & Street 1989; Heifetz, Maor & Guha 2020). As shown in figure 2(*b*), the baroclinic torque is strongest in the vicinity of the inner sphere where the angle between ∇T and $\boldsymbol{g}$ is the largest. The baroclinic torque drives a northward-directed flow along the inner sphere. This results in a large-scale circulation pattern as shown in figure 2(*c*). In steady flows, large-scale circulations induced by baroclinic torque are also reported for side-heated cavity (Jiang, Sun & Calzavarini 2019), stratified flow in a semicylindrical cavity (Kumar & Pothérat 2020), and natural convection in spherical annuli (Scurtu, Futterer & Egbers 2008).

For different n_g, figure 3(*a*) shows the radial ($C_{g,r}g\hat{r}$) and co-latitudinal ($C_{g,\varphi}g\hat{\varphi}$) buoyancy coefficients for $\varepsilon = 0.8$ on the mid-plane of the spherical shell. It shows that g increases monotonically from the north to the south pole when $n_g < 0$. For $n_g > 0$,
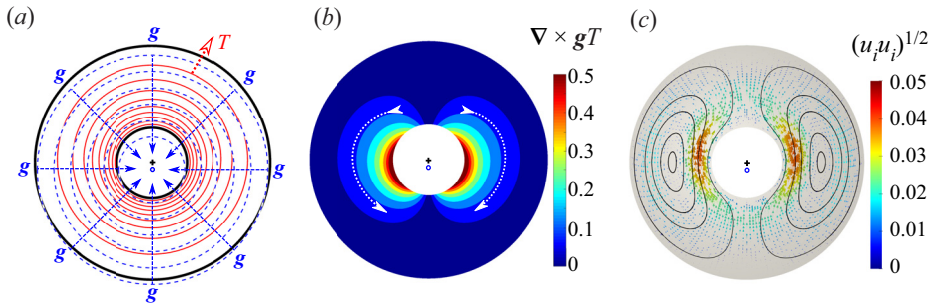
Figure 2. Baroclinic imbalance induces a regular large-scale circulation due to the offset gravity centre towards the south ($\varepsilon = 0.2$, see (2.2)) for a steady flow with $Ra = 10^3$. (*a*) The misalignment of the gravitational potentials (blue dashed circles) and isotherms (red circles) in a meridional cut. The direction is indicated by the blue arrows. (*b*) The corresponding Boussinesq baroclinic torque $\nabla \times \boldsymbol{g}T$. Two dashed arrows correspond to the direction of the baroclinic torque. (*c*) The vector field (coloured by the velocity magnitude) and streamlines (grey curves) of the velocity in the meridian plane.

the opposite trend is observed, while for $n_g = 0$, the gravity is constant as function of the co-latitude location. We keep $Ra = 10^3$ and vary n_g from -2 to 1. The baroclinic torque ($\nabla \times \boldsymbol{g}T$) for $\varepsilon = 0.8$ is shown in figure 3(*b*): $\nabla \times \boldsymbol{g}T$ concentrates in the south polar region when $n_g = -2$, whereas the strongest $\nabla \times \boldsymbol{g}T$ gradually moves to the equator with increasing n_g. The corresponding large-scale circulation is shown in figure 3(*c*); the velocity field strengthens close to the inner sphere and its highest value moves from the south to the equator, which is the same trend as for the baroclinic torque. In addition, the magnitude of the velocity field decreases with increasing n_g due to the decreasing mean buoyancy power ($\overline{\langle gu_rT \rangle}$, see Gastine *et al.* 2015) averaged over the spherical shell.

3.2. *Generation of convective jet and large-scale circulation*

Figure 4 shows the temperature field on the meridional cut in figures 4(*a–d*), the equatorial cut in figures 4(*e–h*, and the surfaces corresponding to the locations of the outer and inner thermal boundary layer heights in figures 4(*i–p*). Figures 4(*b–d*) show that for $\varepsilon \geq 0.05$, the jet ejects hot plumes from the inner sphere towards the outer sphere. When ε is larger, e.g. $\varepsilon \geq 0.4$, thermal plumes preferably ascend northwards along the inner sphere, as shown in figures 4(*o,p*). This happens because the plumes that form along the southern part of the inner sphere move upwards, following the large-scale flow pattern induced by the baroclinic torque; see figure 2(*c*). Consequently, the plumes combine at the northern part of the inner sphere to form the northbound plume towards the outer sphere (figures 4*c,d*). This creates a convective jet impinging on the north pole of the outer sphere, after which thermal plumes descend southwards along the outer sphere, as shown in figures 4(*k,l*). As a result, a limited number of plumes are ejected radially from the hot sphere to the cold sphere in the equatorial region, as shown in figures 4(*g,h*). In addition, we visualize the advection of temperature fluctuation by baroclinic flow $U \cdot \nabla T'$ as shown in figures 4(*q–t*). We find that $U \cdot \nabla T'$ is intense where T is high, which indicates that baroclinic flow works on the temperature perturbation to promote the generation of thermal plumes on the northern side of the sphere. This confirms that the plumes combine at the northern part of the inner sphere to form the northbound plume towards the outer sphere.
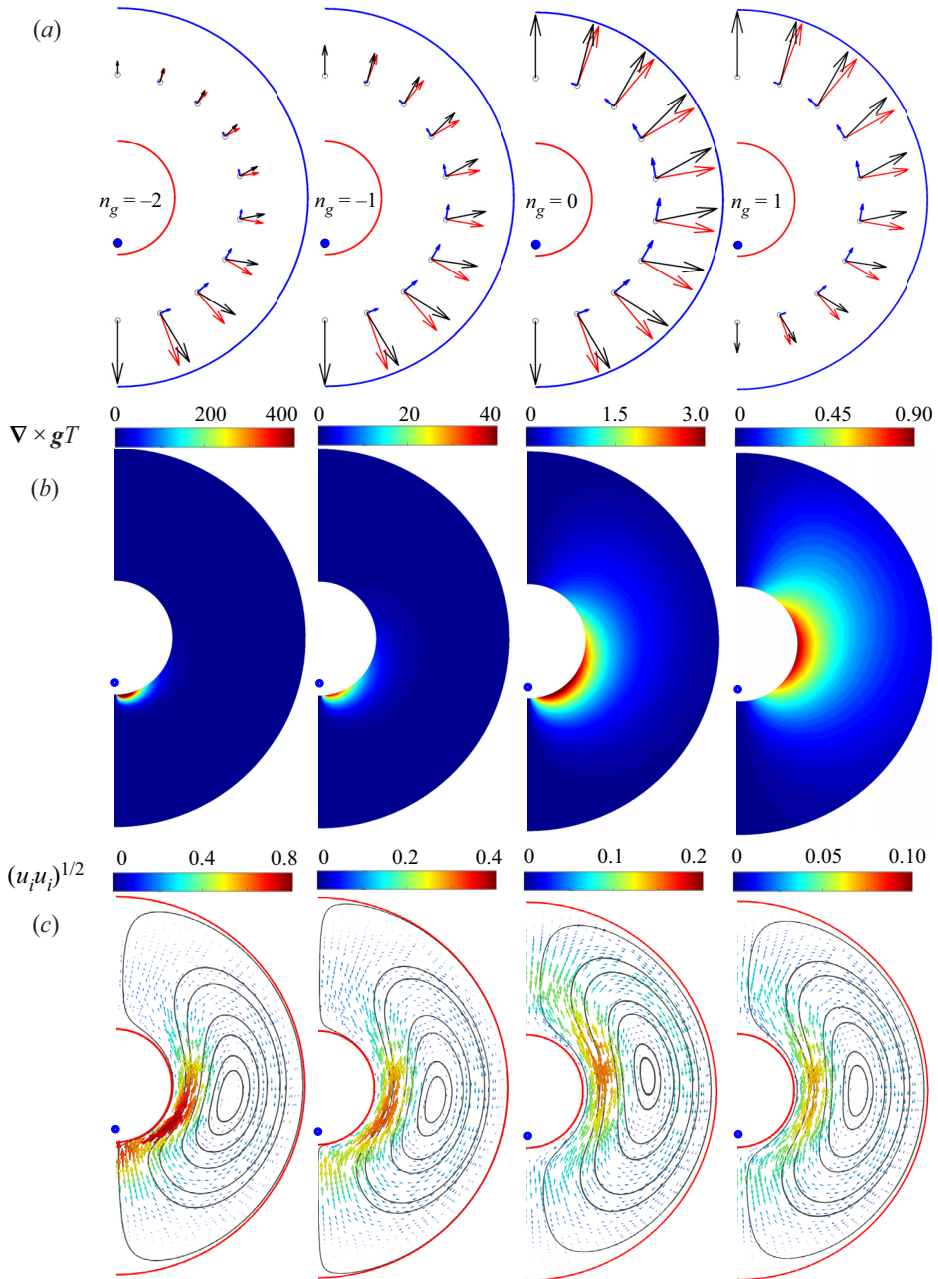
Figure 3. (*a*) The radial ($C_{g,r}g\hat{r}$, red arrow) and co-latitudinal ($C_{g,\varphi}g\hat{\varphi}$, blue arrow) decomposition of buoyancy $g\,\boldsymbol{GP}$ (black arrow) in (2.6) for $\varepsilon = 0.8$. Different panels indicate the buoyancy components on the mid-plane of the spherical shell for $n_g = -2, -1, 0, 1$; see (2.7). The lengths of the arrows are scaled by the co-latitudinal averaged gravity in the mid-plane. (*b,c*) Baroclinic imbalance induces regular large-scale circulation due to the offset gravity centre $\varepsilon = 0.8$ for a steady flow with $Ra = 10^3$ and different gravity profiles. (*b*) The Boussinesq baroclinic torque $\boldsymbol{\nabla} \times \boldsymbol{g}T$ in a meridional cut. (*c*) The vector field (coloured by the velocity magnitude) and streamlines (grey curves) of the velocity in the meridian planes.
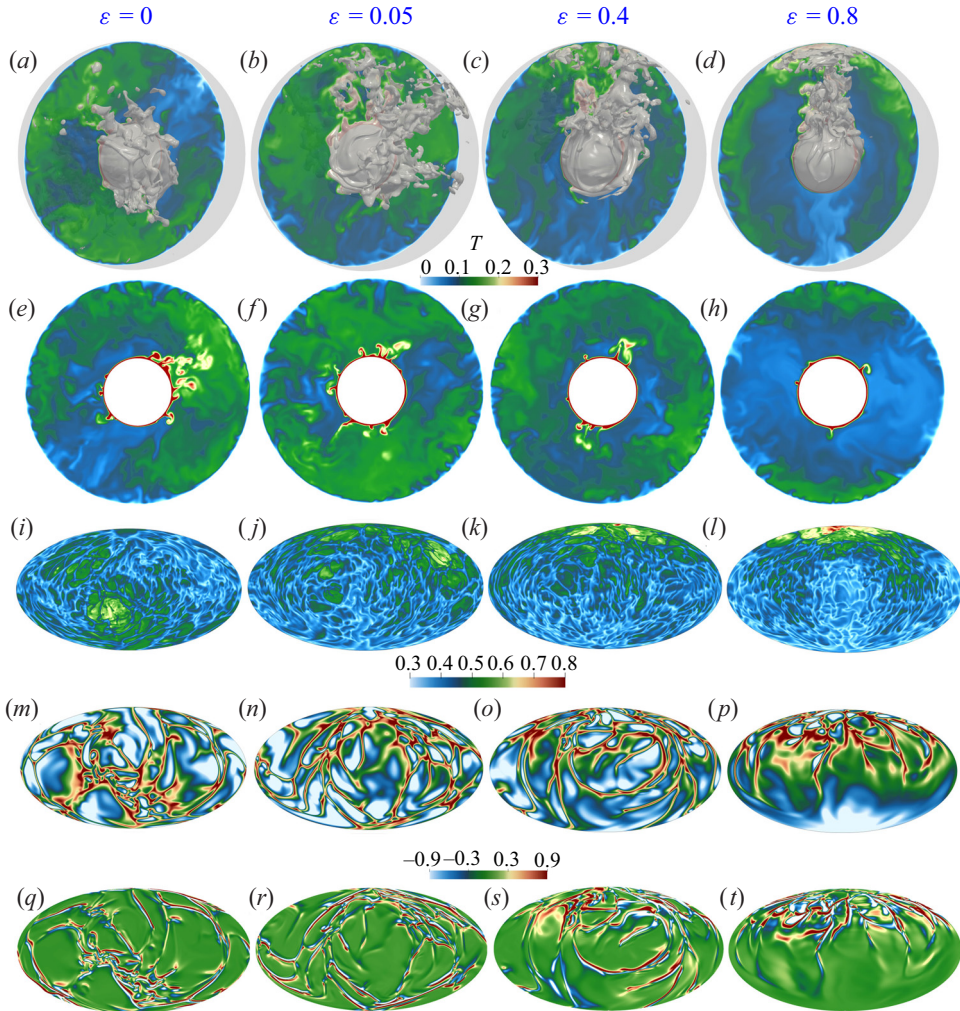
Figure 4. (*a–p*) Snapshots of the temperature fields for $Ra = 10^8$, $n_g = 0$ and $\varepsilon = 0, 0.05, 0.4, 0.8$. (*a–d*) Meridional cut and temperature isosurface for $T = 0.2$. (*e–h*) Temperature field in the equatorial plane, and (*i–l,m–p*) temperature field at the outer (inner) thermal boundary layer heights along the inner and outer spheres, displayed in hammer projections. (*q–t*) Advection of temperature fluctuation by the baroclinic flow $U \cdot \nabla T'$ at the outer thermal boundary layer height.

We compare the unsteady flow fields for $\varepsilon = 0.01$ and 0.05, and different Ra, in figures 5(*a*) and 5(*b*), respectively. The $Ra = 10^3$ cases are shown as reference in the leftmost panel. For the very small $\varepsilon = 0.01$ in figure 5(*a*), the upward convective jet is the strongest for $Ra = 10^7$. However, the convective jet and meridional circulation are weakened significantly for large $Ra = 10^8$. For $\varepsilon = 0.05$, figure 5(*b*) shows that the convective jet is the strongest for $Ra = 10^6$. Again, the convective jet weakens with increasing Ra. In figure 5(*c*), we compare different ε for $Ra = 10^8$. As expected, the convective jet is enhanced significantly with increasing ε. However, the shape of the large-scale circulation is almost unchanged for $\varepsilon \leq 0.4$. When ε increases to 0.8, the large-scale circulation becomes a crescent shaped circulation, which results in its centre moving northwards.
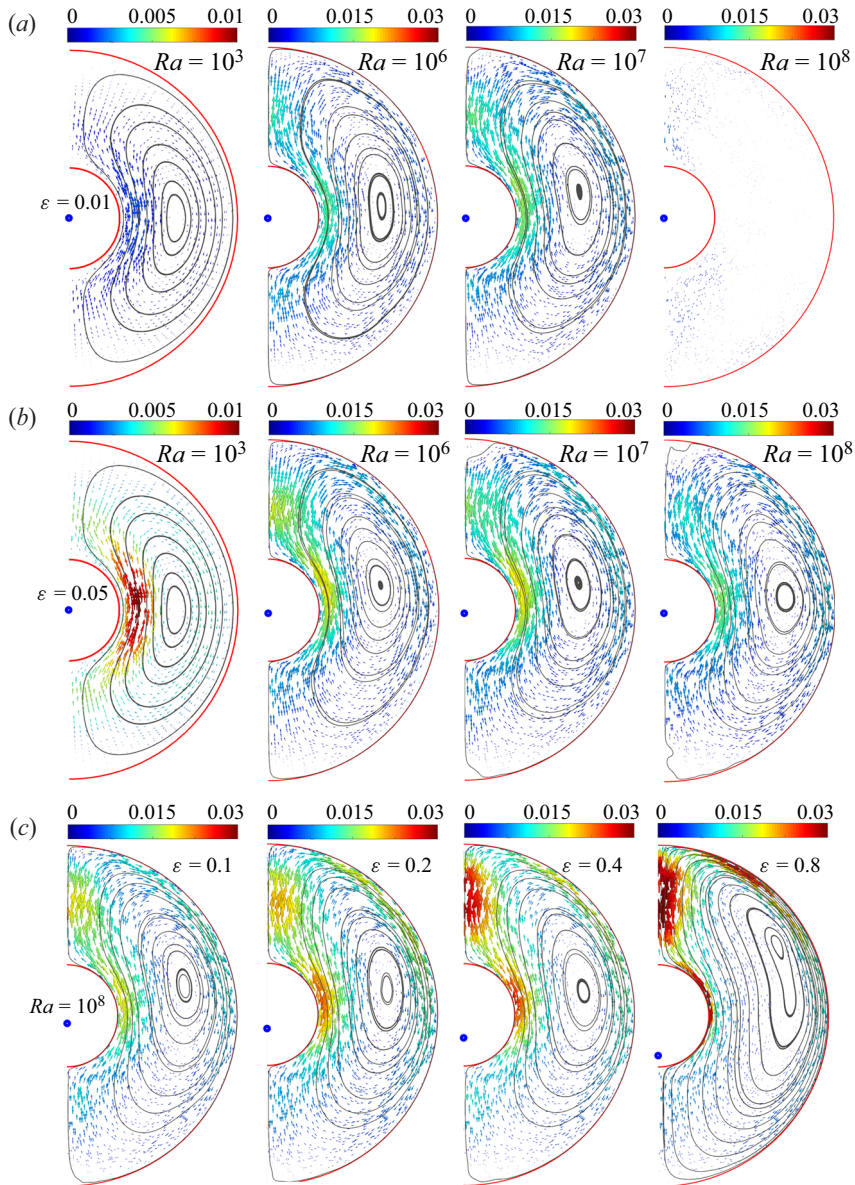
Figure 5. The vector field (coloured by the velocity magnitude) and streamlines (grey curves) of the longitudinal and time-averaged velocity in the meridian plane for: (a) $\varepsilon = 0.01$, and (b) $\varepsilon = 0.05$, with increasing $Ra = 10^3$ (steady flow), $Ra = 10^6$, $Ra = 10^7$ and $Ra = 10^8$; (c) $Ra = 10^8$ and $n_g = 0$ with increasing $\varepsilon = 0.1, 0.2, 0.4, 0.8$.

3.3. Modal analysis to identify large-scale structures

When the gravity centre is moved towards the south pole (increasing ε), the total turbulent kinetic energy (TKE), which is defined as

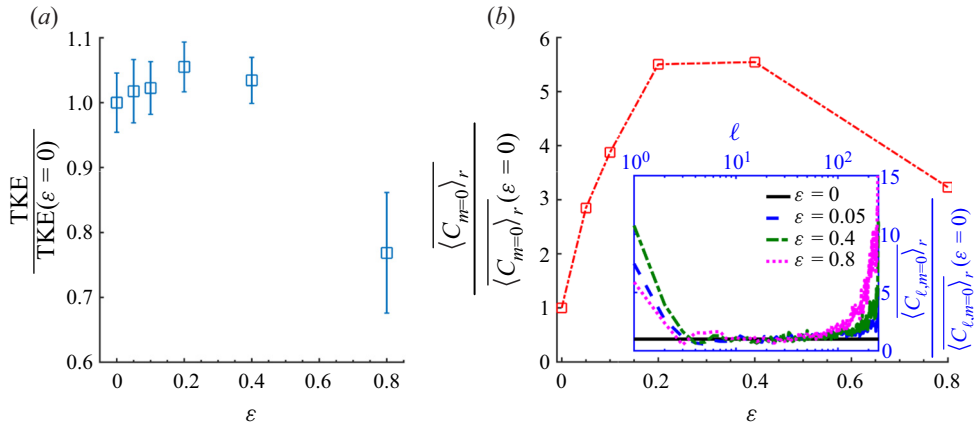$$\mathrm{TKE} = \frac{1}{2}\frac{Ra}{Pr}\overline{\langle u_i u_i \rangle}, \quad i = 1, 2, 3, \tag{3.1}$$

Figure 6. (*a*) Volume-averaged TKE(ε)/TKE($\varepsilon = 0$) as a function of ε for $Ra = 10^8$ and $n_g = 0$. The error bars indicate the corresponding standard deviations. (*b*) Plot of $\langle C_{m=0} \rangle$ of TKE for $\ell > 0$, normalized by $\langle C_{m=0} \rangle$ for $\varepsilon = 0$. The inset shows $\langle C_{\ell,m=0} \rangle$, normalized by $\langle C_{\ell,m=0} \rangle$ for $\varepsilon = 0$, as a function of the spherical harmonic order ℓ, for different ε.

first increases slightly ($\varepsilon \leq 0.4$) and then decreases considerably ($\varepsilon = 0.8$) (see figure 6*a*). To study the effect of the off-centre gravity on the distribution of TKE, we perform a modal analysis of the flow. In spherical coordinates, a surface spherical harmonic function is the expansion of plane waves, where the order m and degree ℓ represent the wavenumbers along the longitudinal and co-latitudinal directions, respectively. Here, we define the power spectrum on a spherical surface as

$$C_{\ell,m} = a_{\ell,m}^2 + b_{\ell,m}^2, \tag{3.2}$$

where $a_{\ell,m}$ and $b_{\ell,m}$ are the spherical harmonics expansion coefficients, which are detailed in Appendix C. We define the power spectrum in the longitudinal direction as

$$C_m = \frac{1}{n - m + 1} \sum_{\ell=m}^{n} C_{\ell,m}, \quad n = \min(N_\varphi - 1, (N_\theta + 1)/2), \tag{3.3}$$

where N_φ and N_θ represent the numbers of grid points in the co-latitudinal and longitudinal directions, respectively. Radial integration and temporal averaging are used to obtain $\overline{\langle \cdots \rangle_r}$. The large-scale circulation is represented by ($m = 0, \ell > 0$) modes as demonstrated in Appendix C.

Figure 6(*a*) shows that the average TKE is almost unchanged for $\varepsilon \leq 0.4$, but the distribution among the different modes is changed. As we have seen in figure 5, a large-scale circulation is formed when $\varepsilon \geq 0.05$ for $Ra = 10^8$. Figure 6(*b*) shows that the axisymmetric ($m = 0$) mode, which indicates the large-scale mode, increases strongly with ε. For $\varepsilon = 0.8$, both the $m = 0$ mode and the total TKE decrease sharply, while it is still enhanced compared with $\varepsilon = 0$. Interestingly, only a small gravity centre offset ($\varepsilon \geq 0.05$) is required to form the convective jet and the corresponding meridional circulation for $Ra = 10^8$. The inset of figure 6(*b*) shows the distribution of the $m = 0$ mode over the different co-latitudinal structures ($\overline{\langle C_{\ell,m=0} \rangle_r}$), which shows that the large-scale circulation is dominated by the co-latitudinal modes with $\ell \leq 3$. With increasing ε, $\overline{\langle C_{\ell,m=0} \rangle_r}$ is enhanced for low ($\ell \leq 3$) and high ($\ell \geq 70$) wavenumbers, compared with $\varepsilon = 0$.
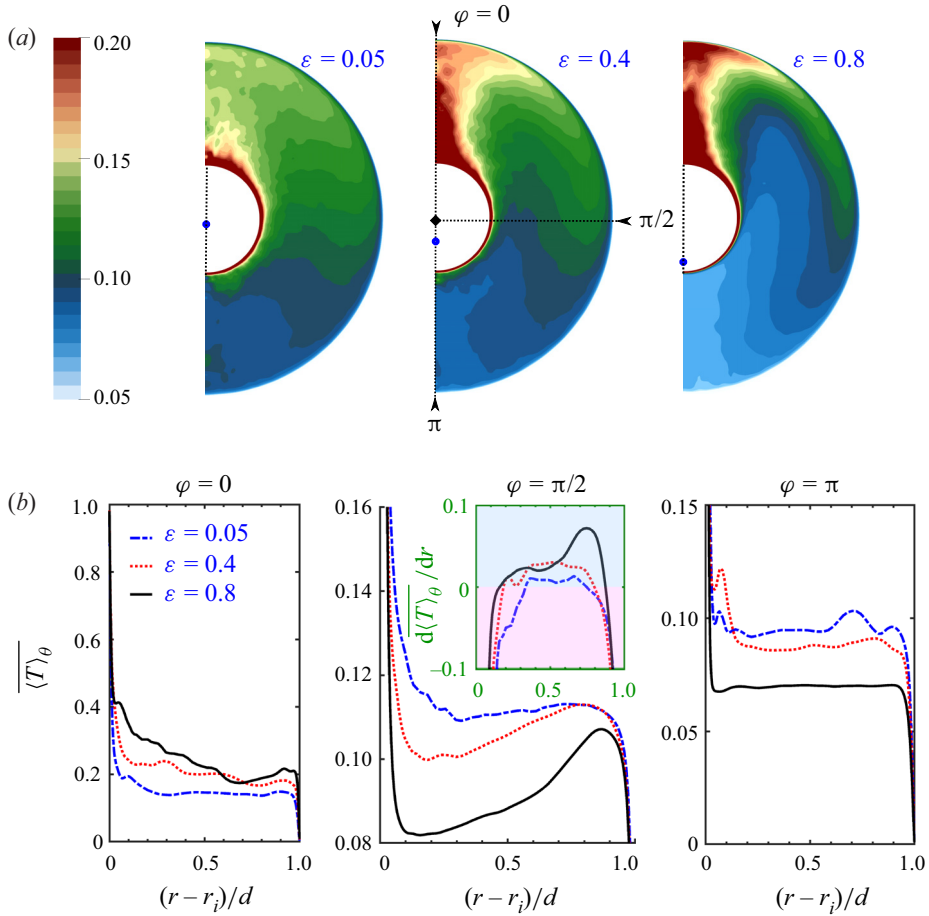
Figure 7. (a) Mean temperature $\overline{\langle T \rangle_\theta}(r, \varphi)$ averaged over time and longitudinal direction shown in the meridian plane for $\varepsilon = 0.05$, 0.4 and 0.8. (b) Mean temperature profiles $(\overline{\langle T \rangle_\theta}(r))$ at three co-latitudes for $\varphi = 0$, $\pi/2$ and π, respectively. The inset for $\varphi = \pi/2$ shows the temperature gradient $d\overline{\langle T \rangle_\theta}(r)/dr$.

3.4. *Effect of large-scale flow on heat transfer distribution*

As we have shown above, the gravity centre offset influences strongly the flow structures. This raises the question of how the local temperature profiles and heat fluxes are affected. Figure 7(a) shows the mean temperature in the meridian plane. For $\varepsilon = 0$, the temperature is uniform in the co-latitude direction. However, with increasing ε, the effect of the north-pole convective jet, which brings hot fluid from the inner to the outer sphere, becomes more pronounced. The effect of the jet is more visible in figure 7(b), which shows the temperature profiles at selected angular positions in the co-latitudinal direction. Most of the temperature drop occurs in the thermal boundary layer regardless of ε and φ. However, for $\varepsilon = 0.4$ and 0.8, the positive temperature gradient $(d\overline{\langle T \rangle_\theta}/dr)$, observed at $\varphi = \pi/2$ and shown in the inset, indicates some thermal stratification in the bulk region.

Next, we examine how the local heat fluxes depend on ε. Figure 8 shows the Nusselt number along the inner $Nu_i(\varphi)$ and outer $Nu_o(\varphi)$ spheres. It is observed that the local heat fluxes on the outer sphere decrease from $\varphi = 0$ (north pole) to $\varphi = \pi$ (south pole), whereas the opposite trend is observed on the inner sphere. This happens because the hot convective
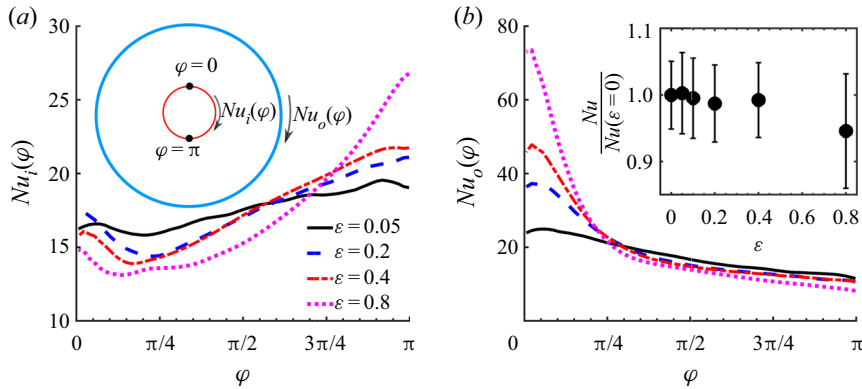
942 A21-12

Figure 8. Nusselt number Nu on (a) the inner sphere and (b) the outer sphere, as functions of the co-latitudinal direction for $Ra = 10^8$ and $n_g = 0$. The inset of (b) shows $Nu(\varepsilon)/Nu(\varepsilon = 0)$ as a function of ε. The error bars represent standard deviations. We note that the error bars for standard errors are smaller than the size of the symbols, which are representative for the uncertainty in the presented global Nusselt values.

jet impinges on the outer boundary layer, resulting in a thinner thermal boundary layer and larger heat flux than without the jet. On the inner sphere, the formation of the convective jet reduces temperature gradients, and therefore the heat transport, at the north pole of the inner sphere, as shown in figure 7(a). Surprisingly, the formation of the large-scale circulation and corresponding non-uniform heat flux distribution has a limited influence on the overall heat flux, which globally is not sensitive to the large-scale dynamics in the flow (Ahlers *et al.* 2009) (see inset in figure 8b), although some reduction in the heat transport is observed for $\varepsilon = 0.8$ when the flow becomes stratified more thermally.

3.5. *Effect of Ra and gravity profile*

So far, we have focused on the effect of the gravity centre offset on the flow structures. In this subsection, instead, we show that convective jet and large-scale flow structures are formed for a wide range of n_g and Ra, and that the control parameters modify significantly the intensity of the large-wavelength structures. However, as we have seen above, the global heat flux depends only weakly on ε in the considered parameter regime.

Figures 9(a–d) show visualizations of the convective jet for $Ra = 10^7$, $\varepsilon = 0.4$, and different gravity profiles. The figures show that the convective jet forms with $u_r > 0$ in the north pole region when the gravity centre shifts to the south. As expected, the jet becomes more turbulent when n_g is decreased, as this increases the mean buoyancy power over the spherical shell. As shown previously in figure 3(a), the co-latitudinal buoyancy component $C_{g,\varphi}g\hat{\varphi}$ points to the north pole in all circumstances. However, the radial buoyancy coefficient $C_{g,r}g\hat{r}$ is strongly dependent on the co-latitude. It is well accepted that the stronger radial velocity component tends to induce more intense thermal plumes. However, the convective jet is still observed in the north pole region rather than the south pole region when $n_g = -2$, as shown in figure 9(d). This confirms that the large-scale circulation is a result of the baroclinic imbalance due to the misalignment of the gravity isopotential and isothermal lines, which is indicated by steady flows shown in figures 3(b,c).

The corresponding $Re_{rms}(r)$, presented in figure 10(a), shows that the turbulent intensity is enhanced greatly with decreasing n_g. This reveals that the flow becomes more
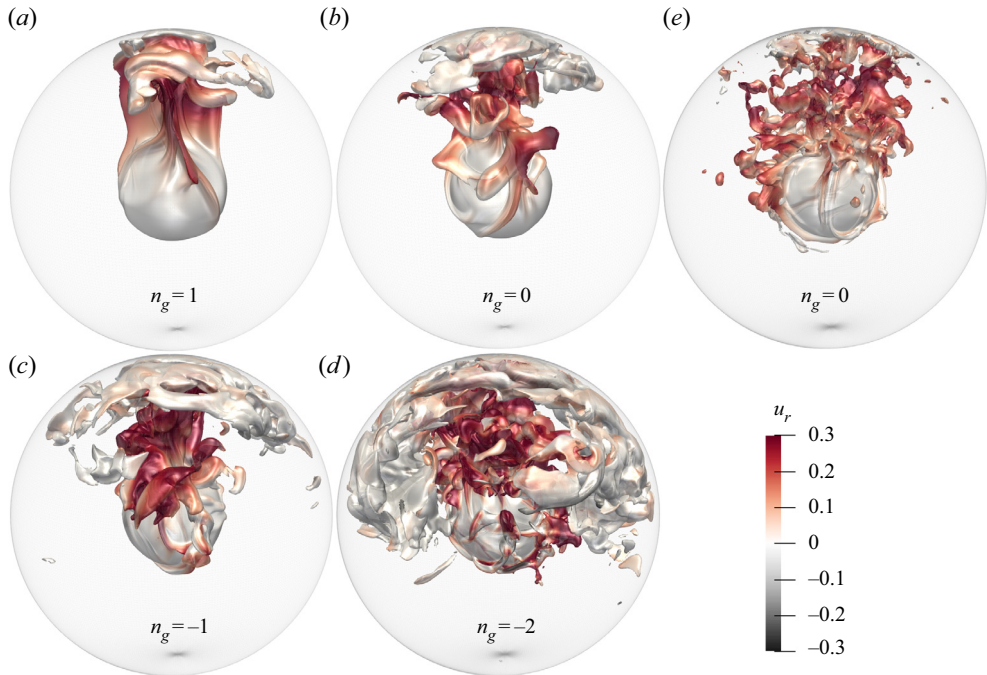
Figure 9. (*a–d*) Instantaneous isosurfaces of $T = 0.2$ for different gravity distributions from $n_g = 1$ to $n_g = -2$ (see (2.7)) for $Ra = 10^7$ and $\varepsilon = 0.4$. Panel (*e*) shows $Ra = 10^8$, $n_g = 0$ and $\varepsilon = 0.4$, for comparison. The colour indicates u_r at the isosurface. (Two movies for $Ra = 10^7$, $n_g = 0$ and $\varepsilon = 0.8$ are provided; see supplementary movies 1 and 2.)

turbulent when n_g decreases, due to the increased buoyancy power over the volume. Correspondingly, figure 10(*b*) shows that the TKE spectrum of $\overline{\langle C_m \rangle}_r$ increases for all wavenumbers. We note that $\overline{\langle C_{m=0} \rangle}_r$, which dominates TKE and indicates the strength of the large-scale circulation, increases with decreasing n_g. With increasing Ra from 10^7 to 10^8, the normalized $Re_{rms}(r)$ is enhanced as shown in figure 10(*c*). As shown in figure 10(*d*), the enhancement happens for all wavenumbers, especially for the high wavenumber structures. Thus for a constant $\varepsilon = 0.4$, the large-scale circulation is more energetic for higher Ra and smaller n_g, due to the increased mean buoyancy power over the volume and the relatively stronger baroclinic torque as indicated in figures 3(*b,c*).

The generation of large-scale structures can induce highly non-uniform co-latitudinal heat flux distribution. We showed previously that the global heat transfer is relatively insensitive to ε for $n_g = 0$ and $Ra = 10^8$. Figure 11 shows that a similar trend is observed for different n_g and Ra. In particular, for $\varepsilon \leq 0.8$, the difference between $Nu(\varepsilon > 0)$ and $Nu(\varepsilon = 0)$ is less than 8 %, which indicates that the effect of the large-scale flow structures on the overall heat transport is relatively limited.

4. Summary and conclusions

We demonstrated using direct numerical simulations that even a small shift of the gravity centre location can introduce pronounced changes in the flow organization and local heat fluxes in spherical RB convection. In the Rayleigh number (Ra) space explored in the present study, we observe the presence of the baroclinic flow, which induces a large-scale
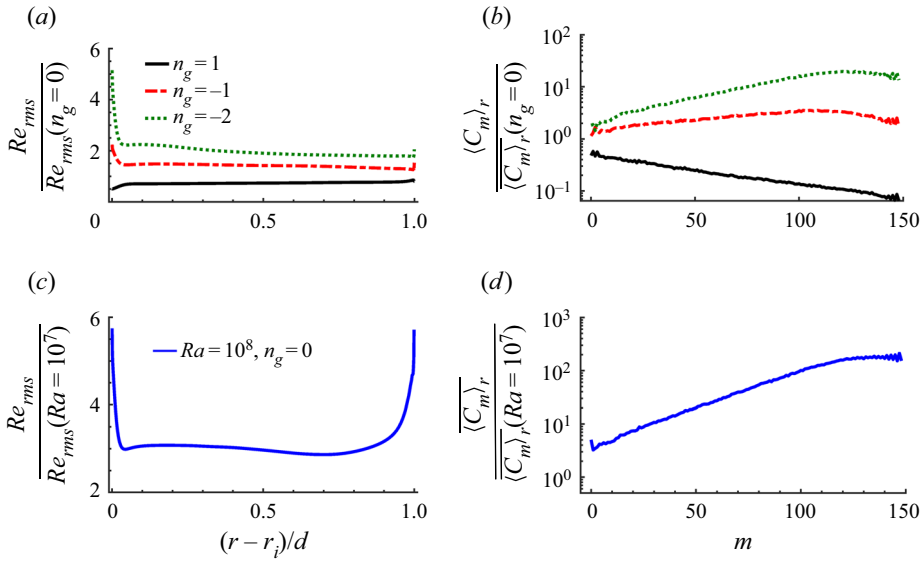
Figure 10. Plots of (a,c) $Re_{rms}(r)$ as function of the gap width, and (b,d) the TKE spectrum of $\overline{\langle C_m \rangle_r}$ for $\varepsilon = 0.4$. (a,b) Here, $Ra = 10^7$ with different n_g; (c,d) here, $n_g = 0$ with different Ra. Figures are normalized by $Ra = 10^7$ with $n_g = 0$. The values of buoyancy power for $Ra = 10^7$ and $n_g = 1, 0, -1, -2$, and $Ra = 10^8$ and $n_g = 0$, are 3.3, 5.55, 12.3, 42.8 and 9.46, respectively.
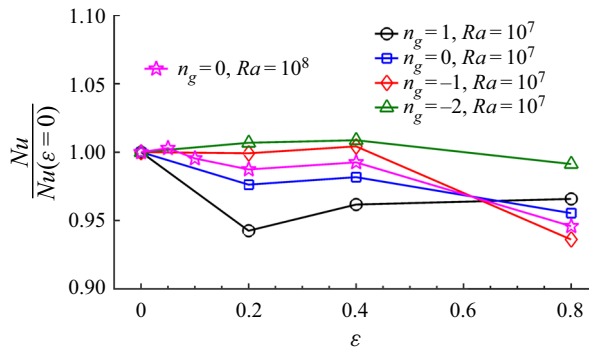

Figure 11. Plots of $Nu(\varepsilon)/Nu(\varepsilon = 0)$ as a function of ε for different Ra and gravity profiles n_g; see (2.7).

circulation and jet for $\varepsilon \geq 0.05$. However, for very small $\varepsilon = 0.01$ and large $Ra = 10^8$, the baroclinic flow is weakened significantly due to the dominance of the strong convective flow. In turbulent flows with $\varepsilon \geq 0.05$, a strong convective jet on the northern side of the inner sphere is formed, which leads to hot/cold fluid going towards the north/south along the inner/outer sphere. The formation of the large-scale circulations has been confirmed by modal analysis. Due to the large-scale flow organization, the heat transfer at the inner and outer sphere is highly non-uniform. In particular, around the north pole, the heat flux is enhanced on the outer sphere due to the impingement of the convective jet, while the formation of the convective jet at the north pole of the inner sphere reduces temperature gradients, and therefore the local heat transport. However, surprisingly, the global heat flux is relatively insensitive to the gravity centre shift. These findings do not seem to depend much on Ra (over our explored range) or the particular gravity profile.

G. Wang, L. Santelli, R. Verzicco, D. Lohse and R.J.A.M. Stevens

Author ORCIDs.
- Guiquan Wang https://orcid.org/0000-0003-4753-7676;
- Roberto Verzicco https://orcid.org/0000-0002-2690-9998;
- Detlef Lohse https://orcid.org/0000-0003-4138-2255;
- Richard J.A.M. Stevens https://orcid.org/0000-0001-6976-5704.

Appendix A. Buoyancy components of off-centre gravity

The two-step transformation of a vector $\boldsymbol{GP}$ in Cartesian coordinates xyz to spherical coordinates $\varphi\theta r$ $(x''y''z'')$ is shown in figure 12. A random fixed point $G(x_G, y_G, z_G)$ is representing the gravity centre location. The other random point, $P(r\sin\varphi\cos\theta, r\sin\varphi\sin\theta, r\cos\varphi)$, is a moving point representing a fluid parcel. Initially, both P and G are in Cartesian coordinates xyz. Using two steps, we will transfer $\boldsymbol{GP}$ to spherical coordinates $\varphi\theta r$ $(x''y''z'')$.

(i) Rotating xyz to $x'y'z'$ about z by an angle θ using the right-hand side rule. The corresponding rotation matrix is

$$R_z(\theta) = \begin{bmatrix} \cos\theta & -\sin\theta & 0 \\ \sin\theta & \cos\theta & 0 \\ 0 & 0 & 1 \end{bmatrix}. \tag{A1}$$

(ii) Rotating $x'y'z'$ to $x''y''z''$ about y' by an angle φ using the right-hand side rule. The corresponding rotation matrix is

$$R_y(\varphi) = \begin{bmatrix} \cos\varphi & 0 & \sin\varphi \\ 0 & 1 & 0 \\ -\sin\varphi & 0 & \cos\varphi \end{bmatrix}. \tag{A2}$$

After the above two steps we obtain that $x''y''z''$ overlaps with $\varphi\theta r$. The transformation matrix $\mathcal{M}_{\theta\varphi}$ from $\boldsymbol{GP}_{xyz}$ to $\boldsymbol{GP}_{x''y''z''}$ is defined by

$$\mathcal{M}_{\theta\varphi} = R_z(\theta) \times R_y(\varphi) = \begin{bmatrix} \cos\theta & -\sin\theta & 0 \\ \sin\theta & \cos\theta & 0 \\ 0 & 0 & 1 \end{bmatrix} \begin{bmatrix} \cos\varphi & 0 & \sin\varphi \\ 0 & 1 & 0 \\ -\sin\varphi & 0 & \cos\varphi \end{bmatrix}$$

$$= \begin{bmatrix} \cos\varphi\cos\theta & -\sin\theta & \sin\varphi\cos\theta \\ \cos\varphi\sin\theta & \cos\theta & \sin\varphi\sin\theta \\ -\sin\varphi & 0 & \cos\varphi \end{bmatrix}. \tag{A3}$$
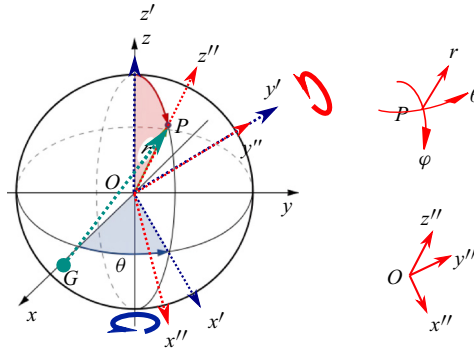
Figure 12. Schematic figure of the two-step transformation of a vector $\boldsymbol{GP}$ in Cartesian coordinates xyz to a spherical coordinates $\varphi\theta r$ $(x''y''z'')$ frame. Circular arrows about the z- and y'-axes show rotation axes.

In the Cartesian coordinate frame, $\boldsymbol{GP}_{xyz} = (r \sin\varphi \cos\theta - x_G, \ r \sin\varphi \sin\theta - y_G, \ r \cos\varphi - z_G)$. Using the above transformations, we find that $\boldsymbol{GP}$ in spherical coordinates $x''y''z''$ is

$$\boldsymbol{GP}_{x''y''z''} = \boldsymbol{GP}_{xyz} \times \mathcal{M}_{\theta\varphi} = (-x_G \cos\varphi \cos\theta - y_G \cos\varphi \sin\theta + z_G \sin\varphi,$$
$$x_G \sin\theta - y_G \cos\theta, \ r - x_G \sin\varphi \cos\theta - y_G \sin\varphi \sin\theta - z_G \cos\varphi). \quad (A4)$$

In the dimensionless equations for the velocity $\boldsymbol{u}$, the buoyancy term is given by $gT \, \boldsymbol{GP}/L_{GP}$, where

$$L_{GP} = |\boldsymbol{GP}| = \sqrt{(r \sin\varphi \cos\theta - x_G)^2 + (r \sin\varphi \sin\theta - y_G)^2 + (r \cos\varphi - z_G)^2}. \quad (A5)$$

The three components in the $\hat{\varphi}$, $\hat{\theta}$ and $\hat{r}$ directions can be decomposed as

$$\left.\begin{aligned}
C_{g,\theta} &= (x_G \sin\theta - y_G \cos\theta)/L_{GP}, \\
C_{g,r} &= (r - x_G \sin\varphi \cos\theta - y_G \sin\varphi \sin\theta - z_G \cos\varphi)/L_{GP}, \\
C_{g,\varphi} &= (-x_G \cos\varphi \cos\theta - y_G \cos\varphi \sin\theta + z_G \sin\varphi)/L_{GP}.
\end{aligned}\right\} \quad (A6)$$

Appendix B. Code validations

We validated extensively our code against the results presented by Gastine *et al.* (2015), who performed a systematic parameter study for spherical RB convection with $Pr = 1$ covering radius ratios $0.2 \leq \eta \leq 0.95$ for different gravity profiles in table 2. The table shows that Nu and the volume-averaged Reynolds number Re_{rms} agree within 2 % with the results from Gastine *et al.* (2015) for all cases. To ensure that the off-centre gravity is implemented correctly, we verified that the flow dynamics for the same L_{OG} (see figure 1) are identical for five different gravity centre locations. The last five rows of table 2 confirm that both Nu and Re_{rms} obtained from these simulations are consistent.

Appendix C. Spectral analysis in spherical coordinates

This appendix describes the spectral analysis procedure used in this study. For further reading on this topic, we refer to pp. 122–145 of MacRobert (1947). In planar configurations, Fourier transformations can be applied when performing spectral analysis.

Ra	η	n_g	$G(\theta, r, \varphi)$	N_θ, N_r, N_φ	Nu	Nu(ref)	Re_{rms}	Re_{rms}(ref)
7×10^6	0.3	1	O	181, 73, 181	6.42	6.40	282.2	287.2
	0.3	0	O	181, 73, 181	8.19	8.15	377.5	377.8
3×10^7	0.3	1	O	251, 93, 163	9.39	9.38	592.0	595.5
5×10^6	0.35	1	O	257, 55, 257	6.80	6.74	274.8	274.1
3×10^8	0.35	1	O	577, 119, 577	21.47	21.23	1815.6	1824.8
5×10^6	0.6	0	O	257, 71, 257	11.85	11.68	437.3	442.7
10^6	0.6	−2	O	325, 71, 325	9.02	8.90	255.4	259.2
3×10^4	0.6	−2	O	129, 49, 97	3.42	3.40	44.1	44.0
		−2	$(0, r_i/2, \pi/2)$	129, 49, 97	3.197	—	40.8	—
		−2	$(\pi/2, r_i/2, \pi/2)$	129, 49, 97	3.187	—	40.8	—
		−2	$(0, r_i/2, 0)$	129, 49, 97	3.191	—	41.1	—
		−2	$(\pi/4, r_i/2, \pi/4)$	129, 49, 97	3.182	—	40.9	—
		−2	$(\pi/7, r_i/2, 3\pi/5)$	129, 49, 97	3.186	—	41.0	—

Table 2. Parameters of the spherical RB simulations with $Pr = 1$, which are compared to the results (Nu(ref) and Re_{rms}(ref)) of Gastine *et al.* (2015). Here, $G(\theta, r, \varphi)$ is the gravity centre location, and N_θ, N_r, N_φ indicate the numbers of grid points in the longitudinal, radial and co-latitudinal directions, respectively. The last five simulations for $Ra = 3 \times 10^4$ are used to verify that the coefficients $C_{g,i}$ (see (A 6)) are implemented correctly, by putting the gravity centre G in five different locations with the same L_{OG} (see figure 1).

However, for a spherical configuration, the basis wave functions are found by solving the Laplace equation. Analogous to the complex exponential in planar configuration, the spherical harmonics $Y_\ell^m(\theta, \varphi)$ read

$$Y_\ell^m(\theta, \varphi) = P_\ell^m(\varphi)\, e^{im\theta}, \tag{C1}$$

where ℓ and m ($-\ell \le m \le \ell$) represent the wavenumbers along a meridian and the equatorial plane, respectively. The polar angle φ ranges from 0 to π, and θ is the azimuthal angle, in the range $0 \le \theta \le 2\pi$. Also, $P_\ell^m(\varphi)$ are the associated Legendre functions. For computational purposes, the normalized associated Legendre functions in (C2) are more attractive since $P_\ell^m(\varphi)$ can overflow the computer (Swarztrauber 1979):

$$\bar{P}_\ell^m(\varphi) = \left[\frac{2\ell + 1}{2} \frac{(\ell - m)!}{(\ell + m)!} \right]^{1/2} P_\ell^m(\varphi). \tag{C2}$$

The use of the spherical harmonics for approximating functions on a sphere is motivated by the fact that they form a complete system of orthogonal functions. Therefore, any function $f(\theta, \varphi)$ that is continuous and has continuous derivatives up to second-order may be expanded in an absolutely and uniformly convergent series

$$f(\theta, \varphi) = \sum_{\ell=0}^{\infty} \sum_{m=-\ell}^{\ell} \bar{P}_\ell^m(\varphi) \left(a_{\ell,m} \cos(m\theta) + b_{\ell,m} \sin(m\theta) \right), \tag{C3}$$

where the expansion coefficients are given by

$$a_{\ell,m} = \frac{1}{\pi} \int_0^{2\pi} \int_0^{\pi} f(\theta, \varphi)\, \bar{P}_\ell^m(\varphi) \cos(m\theta) \sin\varphi \, d\theta \, d\varphi, \tag{C4}$$

$$b_{\ell,m} = \frac{1}{\pi} \int_0^{2\pi} \int_0^{\pi} f(\theta, \varphi)\, \bar{P}_\ell^m(\varphi) \sin(m\theta) \sin\varphi \, d\theta \, d\varphi. \tag{C5}$$
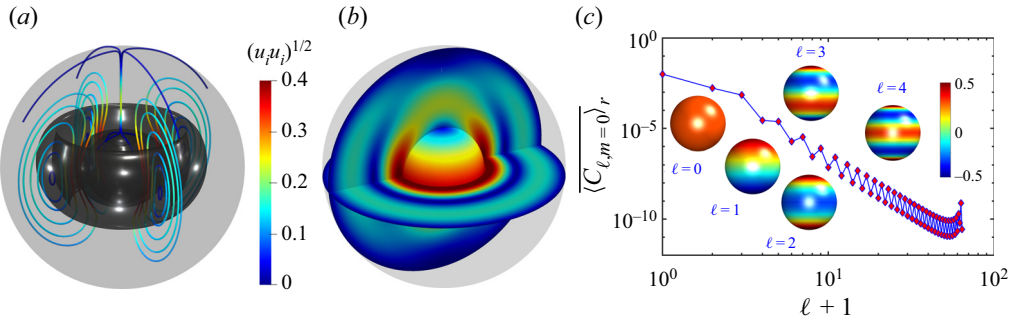
Figure 13. Spectral analysis of a regular large-scale circulation in a steady flow field for $Ra = 10^3$, $n_g = -2$ and $\varepsilon = 0.4$. (*a*) The streamlines (curves coloured by the velocity magnitude) and vortical structures (isosurfaces of the Q-criterion, $Q = 0.006$, coloured black). (*b*) The equatorial cut, meridional cut and radial surface located at $r = r_i + 0.05d$ of the velocity magnitude. (*c*) Plot of $\overline{\langle C_{\ell,m=0} \rangle}_r$ of the velocity field as a function of the spherical harmonic order $\ell + 1$ in logarithmic scale. Also shown is the spherical harmonic basis of $\ell = 0, 1, 2, 3, 4$ for $m = 0$.

The spherical harmonics $Y_\ell^m(\theta, \varphi)$ are orthonormal, so

$$\frac{1}{2\pi} \int_{\varphi=0}^{\pi} \int_{\theta=0}^{2\pi} Y_\ell^m Y_{\ell'}^{m'*} \, \mathrm{d}\Omega = \delta_{\ell\ell'} \, \delta_{mm'}, \tag{C6}$$

where $\delta_{i,j}$ is the Kronecker delta, and $\mathrm{d}\Omega = \sin\varphi \, \mathrm{d}\theta \, \mathrm{d}\varphi$ is the differential solid angle in spherical coordinates. Coefficients (C4) and (C5) are obtained by solving (C3) on a uniform spherical grid by using the SPHEREPACK library (Adams & Swarztrauber 1999).

The power spectrum on a spherical surface $C_{\ell,m}$ and in the longitudinal direction C_m is defined in (3.2) and (3.3), respectively. To demonstrate the formation of ($m = 0, \ell > 0$) modes corresponding to the meridional large-scale circulation, we perform a simulation for $n_g = -2$ and $\varepsilon = 0.4$ with $Ra = 10^3$ (much lower than the critical Rayleigh number when $\varepsilon = 0$). The advantage of using this steady flow is a regular large-scale circulation generated without longitudinal dependent structures ($m \neq 0$), which can be seen from figures 13(*a,b*). The spectrum of the kinetic energy, i.e. $\overline{\langle C_{\ell,m=0} \rangle}_r$, is shown in figure 13(*c*). Except for the mode of ($m = 0, \ell = 0$) representing the mean flow, apparently the large-scale circulation is represented by ($m = 0, \ell > 0$) modes.

REFERENCES

ADAMS, J.C. & SWARZTRAUBER, P.N. 1999 Spherepack 3.0: a model development facility. *Mon. Weath. Rev.* **127** (8), 1872–1878.

AHLERS, G., GROSSMANN, S. & LOHSE, D. 2009 Heat transfer and large scale dynamics in turbulent Rayleigh–Bénard convection. *Rev. Mod. Phys.* **81**, 503–537.

BERCOVICI, D., SCHUBERT, G. & GLATZMAIER, G.A. 1989 Three-dimensional spherical models of convection in the Earth's mantle. *Science* **244** (4907), 950–955.

BUSSE, F. 1970 Differential rotation in stellar convection zones. *Astrophys. J.* **159**, 629.

BUSSE, F. 1975 Patterns of convection in spherical shells. *J. Fluid Mech.* **72** (1), 67–85.

CHILLÀ, F. & SCHUMACHER, J. 2012 New perspectives in turbulent Rayleigh–Bénard convection. *Eur. Phys. J.* E **35** (7), 58.

DESCHAMPS, F., TACKLEY, P.J. & NAKAGAWA, T. 2010 Temperature and heat flux scalings for isoviscous thermal convection in spherical geometry. *Geophys. J. Intl* **182** (1), 137–154.

FUTTERER, B., KREBS, A., PLESA, A.-C., ZAUSSINGER, F., HOLLERBACH, R., BREUER, D. & EGBERS, C. 2013 Sheet-like and plume-like thermal flow in a spherical convection experiment performed under microgravity. *J. Fluid Mech.* **735**, 647–683.

GASTINE, T., WICHT, J. & AURNOU, J.M. 2015 Turbulent Rayleigh–Bénard convection in spherical shells. *J. Fluid Mech.* **778**, 721–764.

HEIFETZ, E., MAOR, R. & GUHA, A. 2020 On the opposing roles of the Boussinesq and non-Boussinesq baroclinic torques in surface gravity wave propagation. *Q. J. R. Meteorol. Soc.* **146** (727), 1056–1064.

IWASE, Y. & HONDA, S. 1997 An interpretation of the Nusselt–Rayleigh number relationship for convection in a spherical shell. *Geophys. J. Intl* **130** (3), 801–804.

JARVIS, G.T., GLATZMAIERAND, G.A. & VANGELOV, V.I. 1995 Effects of curvature, aspect ratio and plan form in two- and three-dimensional spherical models of thermal convection. *Geophys. Astrophys. Fluid Dyn.* **79** (1–4), 147–171.

JIANG, L., SUN, C. & CALZAVARINI, E. 2019 Robustness of heat transfer in confined inclined convection at high Prandtl number. *Phys. Rev.* E **99** (1), 013108.

KUMAR, A. & POTHÉRAT, A. 2020 Mixed baroclinic convection in a cavity. *J. Fluid Mech.* **885**, A40.

LOHSE, D. & XIA, K.-Q. 2010 Small-scale properties of turbulent Rayleigh–Bénard convection. *Annu. Rev. Fluid Mech.* **42**, 335–364.

MACROBERT, T.M. 1947 *Spherical Harmonics: An Elementary Treatise on Harmonic Functions with Applications*. Dover.

O'FARRELL, K.A., LOWMAN, J.P. & BUNGE, H.-P. 2013 Comparison of spherical-shell and plane-layer mantle convection thermal structure in viscously stratified models with mixed-mode heating: implications for the incorporation of temperature-dependent parameters. *Geophys. J. Intl* **192** (2), 456–472.

PUTHENVEETTIL, B.A. & ARAKERI, J.H. 2005 Plume structure in high-Rayleigh-number convection. *J. Fluid Mech.* **542**, 217–249.

SANTELLI, L., ORLANDI, P. & VERZICCO, R. 2021 A finite-difference scheme for three-dimensional incompressible flows in spherical coordinates. *J. Comput. Phys.* **424**, 109848.

SCHLADOW, S., PATTERSON, J. & STREET, R. 1989 Transient flow in a side-heated cavity at high Rayleigh number: a numerical study. *J. Fluid Mech.* **200**, 121–148.

SCURTU, N., FUTTERER, B. & EGBERS, C. 2008 Three-dimensional natural convection in spherical annuli. *J. Phys. Conf. Ser.* **137** (1), 012017.

SHAHNAS, M.H., LOWMAN, J.P., JARVIS, G.T. & BUNGE, H.-P. 2008 Convection in a spherical shell heated by an isothermal core and internal sources: implications for the thermal state of planetary mantles. *Phys. Earth Planet. Inter.* **168** (1–2), 6–15.

SHISHKINA, O., STEVENS, R.J.A.M., GROSSMANN, S. & LOHSE, D. 2010 Boundary layer structure in turbulent thermal convection and its consequences for the required numerical resolution. *New J. Phys.* **12** (7), 075022.

SHISHKINA, O. & WAGNER, C. 2008 Analysis of sheet-like thermal plumes in turbulent Rayleigh–Bénard convection. *J. Fluid Mech.* **599**, 383–404.

SPIEGEL, E.A. 1971 Convection in stars I. Basic Boussinesq convection. *Annu. Rev. Astron. Astrophys.* **9** (1), 323–352.

STEVENS, R.J.A.M., VERZICCO, R. & LOHSE, D. 2010 Radial boundary layer structure and Nusselt number in Rayleigh–Bénard convection. *J. Fluid Mech.* **643**, 495–507.

SWARZTRAUBER, P.N. 1979 On the spectral approximation of discrete scalar and vector functions on the sphere. *SIAM J. Numer. Anal.* **16** (6), 934–949.

TILGNER, A. 1996 High-Rayleigh-number convection in spherical shells. *Phys. Rev.* E **53** (5), 4847.

VERZICCO, R. & ORLANDI, P. 1996 A finite-difference scheme for three-dimensional incompressible flows in cylindrical coordinates. *J. Comput. Phys.* **123** (2), 402–414.

YANAGISAWA, T., KAMEYAMA, M. & OGAWA, M. 2016 Numerical studies on convective stability and flow pattern in three-dimensional spherical mantle of terrestrial planets. *Geophys. J. Intl* **206** (3), 1526–1538.

YANAGISAWA, T. & YAMAGISHI, Y. 2005 Rayleigh–Bénard convection in spherical shell with infinite Prandtl number at high Rayleigh number. *J. Earth Simulator* **4**, 11–17.

ZHOU, Q. & XIA, K.-Q. 2010 Physical and geometrical properties of thermal plumes in turbulent Rayleigh–Bénard convection. *New J. Phys.* **12** (7), 075006.